Processing and luminescence of Eu/Dy-doped $Sr_2MgSi_2O_7$ glass-ceramics

L.Fernández-Rodríguez[a], D.Levy[b], M.Zayat[b], J.Jiménez[c], G.C.Mather[a], A.Durán[a], M.J.Pascual[a]

a *Ceramics and Glass Institute (CSIC), C/ Kelsen 5, Campus de Cantoblanco, 28049, Madrid, Spain*
b *Material Science Institute of Madrid (CSIC), C/ Sor Juana Inés de la Cruz, 3, Campus de Cantoblanco, 28049, Madrid, Spain*
c *GdS Optronlab, Ed. LUCIA, Paseo de Belén, 19, Universidad de Valladolid, 47011 Valladolid, Spain*

Abstract

Glass-ceramics based on the Eu/Dy-doped $Sr_2MgSi_2O_7$ phosphor have been obtained from sintering and crystallization of glass powders. Electric and gas furnaces were employed for glass melting. The doped parent glasses show red emission under excitation of UV light whereas the corresponding glass-ceramics show blue emission. The microstructure of the glass-ceramics and the crystals responsible for the blue emission were observed by scanning electron microscopy-cathodoluminescence. The composition of the crystallised phases and the distribution and incorporation of rare-earth (RE) ions into the crystals and remaining glassy phase were determined by X-ray diffraction and energy dispersive X-ray analysis, respectively.

Photoluminescence emission spectra showed a main peak at 484 nm assigned to the typical Eu^{2+} transitions under excitation at 390 nm in the glass-ceramics. The presence of Dy^{3+} improved persistence in the samples melted in the gas furnace. The glass-ceramics are sensitive to temperature, which modifies both the persistence time and red-blue luminescence.

Keywords: $Sr_2MgSi_2O_7$, Phosphors, Glass-Ceramics, Luminescence Persistence

1. Introduction

Persistent luminescence is an optical phenomenon in which a material emits energy in the visible spectrum for an appreciable time after the excitation source is removed. Depending on the excitation source that starts the emission process, we can define different types of luminescence. The most common is photoluminescence, where the source of excitation are photons absorbed by the material. The photoluminescence is divided into one of two categories depending on the time of emission. Fluorescence where the emission disappears immediately after removal of the excitation source, and

phosphorescence where the emission persists for a time after removal of the excitation source [1]. Persistent luminescence materials have a wide range of applications in several fields, from signalling, computer monitors, ceramic tiles, fluorescent toys, fluorescent lamps or paints, to more advanced technologies such as plasma screens, electroluminescent devices, LEDs and even in biomedicine [2].

For many decades, zinc sulphide doped with copper [3,4] has been the most widely used phosphor; however, its brightness and useful life is quite low for practical purposes. New persistent luminescent phosphors have been intensively investigated in the last twenty years, with persistent emission times ranging from minutes to 12 h [5].

To date, most research on persistent luminescence mechanisms has focused on $SrAl_2O_4:Eu^{2+}$, RE^{3+} materials (RE: rare earth). Europium luminescence has attracted a great deal of attention due to its particular properties. The phosphorescence of Eu^{2+} in most hosts is caused by the 4f → 5d transition. The peaks that appear in the emission spectra of Eu^{2+} depend on its lattice environment and emission can occur at different visible wavelengths [[6], [7], [8]]. Matsuzawa et al. proposed in 1996 a mechanism to explain the persistent luminescence on $SrAl_2O_4$: Eu^{2+}: Dy^{3+} crystals, which is generally accepted to describe the persistent luminescence in Eu^{2+}- and Dy^{3+}- doped aluminates and silicates [9].

The MAl_2O_4 series (M = Ca, Sr, Ba) [10] doped with Eu_2O_3 and Dy_2O_3 are the most studied materials with persistent luminescence. However, $SrAlO_4$: Eu^{2+} without co-doping exhibits considerable residual brightness, indicating that co-doping is not essential to obtain persistent luminescence. Co-doped MAl_2O_4: Eu^{2+} has been simply, efficiently, and cheaply synthesized in several studies. The most widely used method is solid-state reaction at 1300−1400 °C, but sol-gel and microwave routes can also be utilised [11].

Much research has focused on achieving persistent luminescence based on divalent europium as the activator. However, a large number of publications also focus on compounds without Eu^{2+} addition [3] due to the lack of persistent phosphors emitting in the red. Matches with red emission are very desirable for various applications from signalling or paints to their use as tracer particles for live medical images [3].

Abbruscato et al. [12] prepared different samples of $SrAl_2O_4$: Eu^{2+} by firing and observed that excess of aluminium may be incorporated interstitially or create Sr^{2+} vacancies. Matsuzawa et al. [9] observed that co-doping with Dy results in a remarkably intense phosphorescence, and that capture levels must be obtained at the appropriate depth for phosphors to have prolonged phosphorescence at room

temperature. The mechanism proposed by Matsuzawa was modified by Abbruscato [12] to explain the influence of rare-earth co-doping.

Aitasalo et al. [13] focused on the study of different MAl_2O_4: Eu^{2+} (M = Ca and Sr) compounds by solid state reaction. The brightness of Eu^{2+} was enhanced by co-doping with trivalent rare earths. In the mechanism proposed by Aitasalo, the electrons are excited by thermal energy, which requires a close proximity between the vacancies and the luminescence centres [14].

Based on the research of Matsuzawa [9] and Aitasalo, Dorenbos et al. [15]. concluded that the electrons are excited in divalent europium ions. Thermal energy releases trapped electrons, which recombine in a luminescence centre.

In contrast, in the Clabau et al. model [16], there is direct transfer and no migration of electrons through the conduction band as in previous models. Their research also compared the brightness of $SrAl_2O_4$: Eu^{2+} (not co-doped) and co-doped with Dy^{3+}, and noted that the relevant peaks differed in intensity and position, but maintained a very similar shape, so the chemical nature of the trap was not influenced by co-doping.

Recently, silicate-based phosphors doped with rare earths have attracted much attention because of their many advantages compared to sulphide and aluminate phosphors, including high chemical stability, colour variety and water resistance [17,18]. The $Ba_3MgSi_2O_8$ [19] structure can be described as stacked hexagonal perovskite layers. Considering the three different crystallographic locations of $Ba_3MgSi_2O_8$, it can be expected that three Eu^{2+} emission bands will be observed in the luminescence spectrum. $Sr_2MgSi_2O_7$ [20] has a tetragonal host symmetry with a single Sr^{2+} crystallographic site, along with a much more effective persistent luminescence [12,20,21]. Despite the fact that there are many studies of the $Sr_2MgSi_2O_7$ phase, there are few published papers on their luminescent properties [22,23]. Although the luminescence mechanisms are not fully understood, according to some theoretical studies, oxygen vacancies could be responsible for the persistent luminescence [25]. $Sr_2MgSi_2O_7$ phosphors, prepared by high temperature solid state reaction, have been investigated for LED applications [26], due to their long persistence and high chemical stability. Their excitation spectrum is wide, ranging from the UV to the blue region.

The oxidation state of europium has an important role in the persistent luminescence. Eu^{3+} exhibits a red emission that is not persistent, while Eu^{2+} has a blue emission that is persistent [5]. In most papers, these phosphors are obtained in a reducing atmosphere to reduce the Eu^{3+} to Eu^{2+}. However, as shown by Pei et al. [27], selection of a suitable matrix renders a reducing atmosphere to obtain Eu^{2+} unnecessary. They studied SrB_4O_7:

Eu^{2+} and $Sr_2B_5O_9Cl$: Eu^{2+}, and concluded that one of the main factors explaining why Eu^{3+}, introduced as Eu_2O_3, is reduced to Eu^{2+} in non-reducing atmospheres, is the existence of the tetrahedral anionic group BO_4. When trivalent Eu^{3+} ions are incorporated into Sr borates, the only cations that may be substituted are Sr^{2+} ions.
In later works [28], it was confirmed that Eu^{2+} may be obtained without using reducing atmosphere in the presence of tetrahedral anionic groups, such as SiO_4 or AlO_4.
Solid state reaction is mostly employed for the synthesis of these phosphor materials [27]. Other methods which have been used include hydrothermal synthesis [23], electrospinning [29], sol-gel [30], combustion [31], co-precipitation [24], and the newer "Molten Salt" [32] method. Many of these techniques are not compatible with large-scale production and sustainability principles. In addition, the industrial availability of highly crystalline powders normally requires high temperature synthesis, with long processing times, especially for solid-state reaction. Although there are several reports in the literature about preparation of glass-ceramics, it has not been widely explored. Nishiura et al. [33] prepared $M_2MgSi_2O_7$:Eu^{2+} (M = Sr, Ca) glass-ceramics by melting the glass in a reducing atmosphere, using a crucible of graphite powder to improve the reducing effect, with subsequent heat treatment also in reducing conditions. Replacing Sr with Ca results in a broadened emission spectrum, and a shift from 470 to 530 nm, which can be attributed to the change in the environment of the Eu^{2+} ligand field as the size of the M site becomes smaller. The emission colour changes from blue with Sr, to green-yellow with Ca; hence, the emission colour can be tuned on varying the Sr/Ca ratio.
Wondraczek et al. [34] investigated (Sr,Ca)-akermanite $(Ca,Sr)_2MgSi_2O_7$ glass-ceramics doped with europium, employing glucose as reducing agent in the melting process, with final thermal treatment at 750 °C. The emission of the glass presents a Eu^{3+}(red) characteristic band, whereas the glass-ceramic emits with the Eu^{2+} (blue). Characterization by Scanning Electron Microscopy-Cathode-luminescence (SEM-CL) indicated that the crystalline phase is associated with the dominant Eu^{2+} emission, and it is proposed that Eu^{2+} is incorporated in Sr^{2+} sites of the akermanite structure, whereas Eu^{3+} accumulates in the intergranular phase of the glass.
In addition, Nakanishi et al. [21] prepared $BaSi_2O_5$: Eu^{2+} glass-ceramics by melting, obtaining emissions in the range 500–520 nm (green). Recently, Asami et al. [22] prepared co-doped Eu^{2+}/Dy^{3+} $Ba_5Si_8O_{21}$ glass and glass-ceramic samples obtaining a duration of the persistent luminescence over 16 h.

The objective of this paper is the preparation of glass-ceramics with persistent luminescent properties based on silicate phases. The starting glass system was chosen as MgO-SrO-SiO_2 in order to obtain glass-ceramics with $Sr_2MgSi_2O_7$ doped with rare earths which give rise to phosphorescence. Glasses doped with Eu_2O_3 and co-doped with Eu_2O_3 and Dy_2O_3 were melted in electric and gas furnaces to compare both methods and without adding reducing agents. Melting in a gas furnace is of interest to reproduce industrial preparation conditions. Sintering and crystallization processes were investigated by differential thermal analysis (DTA), hot-stage microscopy (HSM) and X-ray diffraction (XRD). The microstructure of the glass-ceramics was observed using SEM-CL and the optical characterization was completed by photoluminescence (PL) measurements. The results are discussed with reference to the processing-structure-property relationships.

2. Experimental procedure

2.1. Glasses and glass-ceramics preparation

Glasses of the same base composition $55SiO_2$-$27SrO$-$18MgO$ mol% (hereafter referred to as undoped, E (melted in electric furnace) and G (melted in gas furnace)) doped with 0.1, 0.5 and 1 mol% Eu_2O_3 and co-doped with 1% Eu_2O_3+0.5 % Dy_2O_3 (mol%) were prepared by melt-quenching from SiO_2 sand (Saint-Gobain, 99.6 %), $SrCO_3$ (Alfa Aesar, 97.5 %), MgO (PanReac, 98 %), Eu_2O_3 (Alfa Aesar, >99.9 %) and Dy_2O_3 (Alfa Aesar, >99.9 %). Batches of 100 g were mixed and stirred in a turbula mixer for one hour to achieve homogenization. The glasses were melted in an electric furnace in a Pt/Rh crucible covered with a Pt lid by firstly calcining at 1300 °C for one hour then melting twice at 1550 °C before pouring onto either a brass mould to obtain glass bars or on water to obtain frits. Alternatively, an uncovered AZS (alumina-zirconia-silica, Al_2O_3–ZrO_2–SiO_2) crucible was used for melting selected compositions doped with 0.5 %Eu_2O_3 mol% and 1%Eu_2O_3+0.5 %Dy_2O_3 mol% in a gas furnace (propane/air). The temperature was maintained at 1300 °C for 15 min, followed by an increase to 1550 °C for 1 h, with final heating to 1600 °C before pouring into water to obtain a frit. Chemical analysis of the glasses was performed by X-ray fluorescence spectroscopy, using a Magic X 2400 spectrometer, PANalytical. The analyses were carried out using the semi-quantitative analysis curve of IQ+, analysing the samples as a pearl (by melting 0.3000 g of sample and 5.5 g of $Li_2B_4O_7$).

The frits were milled in acetone and the powders sieved below 20 μm. Cylindrical pellets (Ø = 2.5 cm) were prepared by pressing the powder into a die (1600Kp during 3 min) before firing in an electrical furnace at 1100 °C (heating and cooling rate 10 °C/min) for 1 h or 1 min in air to obtain the corresponding glass-ceramics.

2.2. Thermal and structural characterization

Small glass samples (12 mm × 8 mm × 5 mm) were cut from the bars and analysed by dilatometry in a Netzsch DIL 402 PC instrument at a heating rate of 5 °C/min. The coefficient of thermal expansion α (CTE) was obtained by a linear fit of the curve in the range 100–500 °C; the glass transition temperature (T_g) and dilatometric softening temperature (T_d) were also determined.
DTA curves were recorded with a SETARAM Setsys Evolution instrument, using samples of particle size < 20 μm up to 1200 °C with heating rates 2, 5, 10, 20 and 30 °C/min; a larger particle size (1–1.5 mm) was also employed to reproduce the bulk crystallization behaviour.

An EM 201 side-view hot-stage microscope (HSM) with image analysis and 1750/15 Leica electric furnace was used to determine the sintering and flow behaviour of the glass powders. Details of the equipment have been reported previously [34,35]. Measurements were conducted in air at a heating rate of 10 °C/min on powder samples with particle size < 20 μm. The temperature was measured with a Pt/Rh (6/30) thermocouple placed under the alumina support and in contact with it. The changes in the area of the samples are associated to different processes and correspond to points of viscosity that were previously determined [36].
The glass-ceramic pellets were milled and sieved to a particle size lower than 60 μm and initially characterized by X-ray diffraction (Bruker D8 Advance) in the range 10–70° 2θ with a step size of 0.02°, employing $CuK_{\alpha 1}$ radiation (λ = 1.54056 Å). Rietveld refinement was employed for the quantification of the crystalline phases present in the selected glass-ceramics E-0.5 Eu, E-1 Eu-0.5Dy and G-1 Eu-0.5Dy (treated at 1100 °C for 1 min) using NaF as internal weight standard according to a previously reported procedure [37,38]. The XRD data for Rietveld refinement were collected on the same diffractometer in the range 10–100 ° (2θ) with a step size of 0.02° and accumulation time of 1.2 s per step with rotation of the sample. The FULLPROF program was used for refinement of the structural models and quantitative analysis [39].

SEM-CL of the same selected glass-ceramic samples was performed on a Hitachi S-3000 N microscope equipped with a vacuum chamber, on excitation with an electron beam of voltage 15–25 kV and a filament intensity of 100 μÅ. The emission spectra were recorded employing a fibre spectrometer with a charge-coupled device (CCD) through an optical fibre, and the corresponding luminescence photographs with an ordinary camera. The instrument is equipped with secondary electron (SE) and backscattered electron (BSE) detectors, an energy dispersive X-ray spectroscope (EDX) Quantax (model XFlash 6I30, Bruker) and a cathode-luminescence system (CHROMA-CL2 Gatan). Samples were compositionally accurate to within the uncertainty in the EDX (∼1 %). Additionally, spectrally resolved CL measurements were carried out at 80 K on a MONO-CL2 system (Gatan) attached to a Field Emission Scanning Electron Microscope (FE-SEM, ZeissLEO 1530). Detection is performed with a photomultiplier for panchromatic images, and a Peltier cooled Si−CCD for spectrally resolved images.

2.3. Optical characterization

The glass-ceramic pellets were observed under UV light (18 W ($\lambda = 365$ nm), I =0.025 mA / cm^2) at different temperatures (0 °C, RT and 130 °C) to check for emission and persistence of phosphorescence.
Fluorometric measurements of the glass-ceramic pellets were performed at 25 °C using an Avantes spectrometer (AvaSpec-ULS2048 L) instrument attached to an Ultra-Low Straylight Fiber Optic VIS/NIR Slit 25-RS spectrometer. A front-surface sample holder for thin-film solid samples was built for data collection and oriented at 60 degrees to the angle of light excitation to minimize scattered light. Appropriate filters were used to eliminate Raleigh and Raman scatter from the emission. Emission spectra were corrected for the wavelength dependence of the 150-Watt Xenon arc excitation, but not for the wavelength dependence of the detection system.

Lifetime measurements were done using an AvaSpec-ULS2048CL-EVO-RS with a CMOS detector operating at an integration time of 150 ms and averaging 5 spectra with a total recording time of 0.75 s. A 365 nm UVP Blak-Ray™ B-100AP High-Intensity lamp, 8.9 mW/cm^2, was used for sample excitation and a fiber-optic switches accessory for automatic shuttering. To enable temperature dependent lifetime measurement, a liquid cooled cryostat was integrated to the sample isolated sample chamber. The temperature was measured by a PT100 sensor placed as closely as possible to the

sample to take into account the heat conductivity of the heat exchanger with an accuracy of ±0.5 °C.

3. Results and discussion

3.1. Thermal and structural properties

Fig. 1 shows the dilatometric curves of the undoped and doped glass compositions. The glass transition temperature, T_g, is around 720 °C and the CTE in the range 100–500 °C is $9.5 \pm 0.5 \times 10^{-6}$ C^{-1}. Both T_g and α increase with increasing dopant content (Table 1).

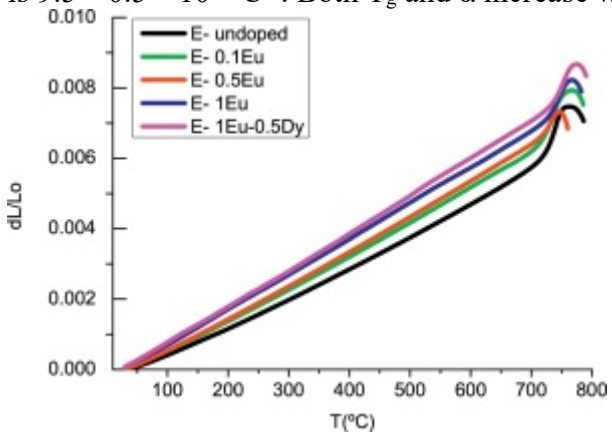

Fig. 1. Dilatometric curves of the E glasses.

Table 1. T_g and CTE (α) of the E glasses determined by dilatometry.

Compositions	T_g (°C) ± 2	$\alpha_{100-500°C}$ (C^{-1}) ±0.5 × 10^{-6}
E-undoped	722	9.1
E-0.1 Eu	722	9.1
E-0.5 Eu	725	9.5
E-1 Eu	734	10.1
E-1 Eu-0.5Dy	741	10.4

Fig. 2a shows DTA scans for the undoped glass with different particle size (<20 μm and 1–1.5 mm). The crystallization peak is better defined for the bigger particle size (simulating the bulk behaviour), but crystallization occurs at a higher temperature. The characteristic crystallization temperatures (T_x, temperature of initial crystallization and T_c, crystallization temperature) are around $T_x \sim 870$ °C and $T_c \sim 940$ °C for the glass with particle size <20 μm and $T_x \sim 940$ °C and $T_c \sim 1000$ °C for the bulk glass. This pronounced difference in the crystallization temperature indicates an important contribution of surface crystallization. The melting peaks appear around 1130 °C.

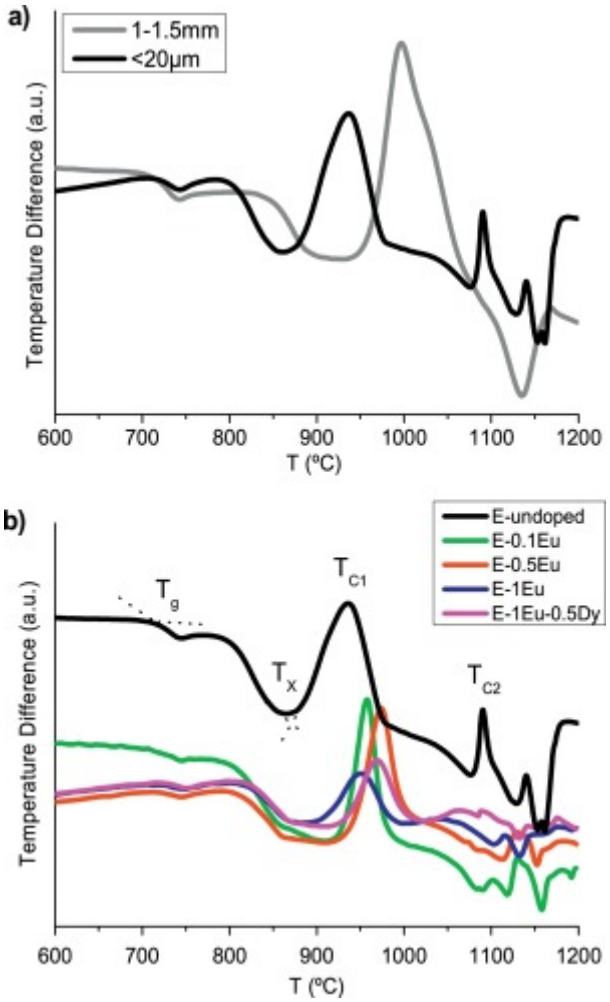

Fig. 2. a) DTA curves of the E undoped glass with different particle size. b) DTA curves of the E doped glasses with different dopant concentrations. Heating rate: 10 °C/min.

Fig. 2b represents the DTA results for samples doped with different dopant concentrations and a particle size < 20 µm. On increasing the europium concentration from 0.1 to 0.5 %, the crystallization peak appears at higher temperature. If the Eu concentration increases to 1%, the crystallization peak shifts to lower temperature and appears less defined. By co-doping (1 Eu-0.5Dy), the crystallization peak occurs at even higher temperature and is better defined. The characteristic crystallization temperatures are around T_x and T_c 900 °C and 950 °C, respectively. These values are in agreement with the temperatures shown previously in Table 2 for the undoped glass with particle size < 20 µm. The increase in dopant concentration decreases the tendency for crystallization.

Table 2. T_g, T_x and T_c of the E undoped glass (ø <20 µm) determined by DTA.

Heating rate	**T_g(°C) ± 7**	**T_x(°C) ± 9**	**Tc_1(°C) ± 9**	**Tc_2(°C) ± 9**
2 °C/min	715	833	910	–

Heating rate	T_g(°C) ± 7	T_x(°C) ± 9	Tc_1(°C) ± 9	Tc_2(°C) ± 9
5 °C/min	716	852	930	1071
10 °C/min	720	870	934	1090
20 °C/min	715	867	954	1090
30 °C/min	723	887	957	1095

The effect of different heating rates on the crystallization temperatures obtained from DTA curves (curves not shown) is illustrated in Table 2 for the E undoped glass. On increasing the heating rate, the nucleation time decreases and, as a result, the crystallization peaks appear at higher temperature.

The kinetic parameters of crystallization were studied by the non-isothermal method at different heating rates. The activation energy of crystallization was determined by considering the dependence of the heating rate with the temperature of crystallization according to Kissinger's equation [40] (1):(1)lnQTc2=-EaRTc+Cwhere Q is the heating rate, T_c is the temperature of the crystallization peak, R is the gas constant (8314 J mol^{-1} K^{-1}), E_a is the activation energy and C is a constant. The linear regression of the $Ln(Q/T_c^2)$ vs. $1000/RT_c$ plot (figure not shown) provides an activation-energy value for crystallization of 579 ± 15 kJ/mol.

The Avrami parameter (n) in the JMA model provides information about the crystallization mechanism that occurs in the glass system. Based on the values of the activation energy, the Avrami parameter was calculated using the Augis-Bennett equation (2):((2))n=2.5RTc2ΔTEawhere ΔT is the width at the centre of the peak.

The value obtained from the Avrami parameter is 1.2, confirming that surface crystallization is the main crystallization mechanism taking place in the samples [41].

Fig. 3 shows DTA curves comparing glasses G-0.5 Eu and E-0.5 Eu. The crystallization peak of G-0.5 Eu appears at higher temperature and is less pronounced. This is mainly due to differences in the final composition between both glasses due to variations in the melting process and type of crucible. Chemical analysis of the glasses, shown in Table 3, indicates higher SrO volatilization when melting in the gas furnace. This glass crystallizes at higher temperature and shows less tendency to crystallize (according to the area of the crystallization peak). In addition, when melting in a gas furnace, the final composition shows impurities from the crucible components which can also affect the crystallization (Al_2O_3, ZrO_2).

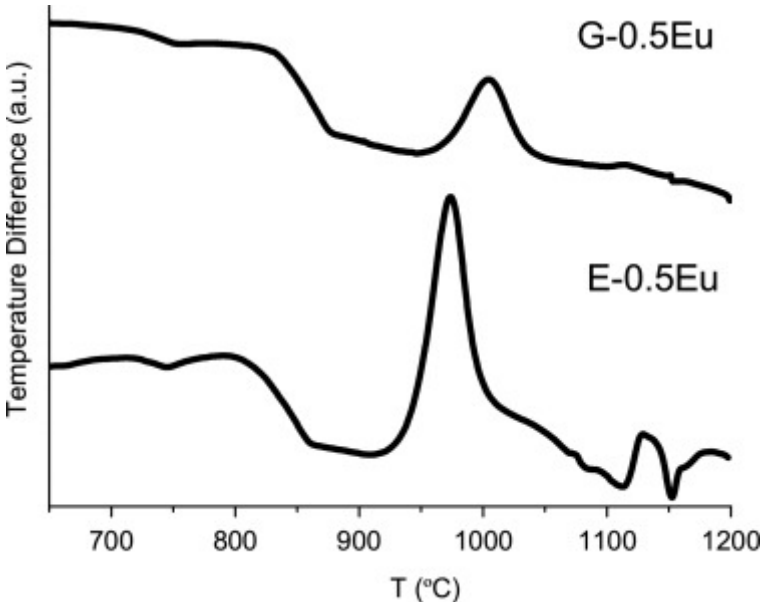

Fig. 3. DTA curves of G-0.5 Eu and E-0.5 Eu glasses. Heating rate: 10 °C/min.

Table 3. Chemical analysis (mol%.) of the glasses melted in gas (G) and electric (E) furnaces.

Glass components	**G-0.5 Eu**	**E-0.5 Eu**	**G-1 Eu-0.5Dy**	**E-1 Eu-0.5Dy**
MgO	19.17	17.51	16.71	19.03
SiO_2	52.63	50.94	56.40	51.68
SrO	24.41	29.82	23.76	26.79
Eu_2O_3	0.50	0.60	1.03	1.12
Dy_2O_3	0	0	0.5	0.33
Al_2O_3	1.63	0.53	1.42	0.51
K_2O	0.15	0.18	0.18	0.21
Na_2O	0.52	0.26	0	0
ZrO_2	0.46	0.16	0	0
CaO	0.16	0	0	0.17
BaO	0.37	0	0	0.15

Fig. 4 shows the results of HSM for glass powders with different dopant concentrations (all glasses melted in electric furnace); sintering and flow temperatures are listed in Table 4. The temperatures of maximum sintering partially overlap with those of the initiation of crystallization which could affect densification (Fig. 2, Table 2). The softening temperature (T_S) is ~ 870 °C for all samples. Generally, samples become spherical around 930 °C, but the sample with 1 Eu does not do so until 1147 °C. All samples reach the half-ball temperature (T_{HB}) at ~1200 °C and then flow. From the HSM and DTA results, a thermal treatment of 1100 °C was chosen to obtain sintering,

crystallization and flow, thereby enabling glass-ceramic pieces or enamels to be prepared as possible final products.

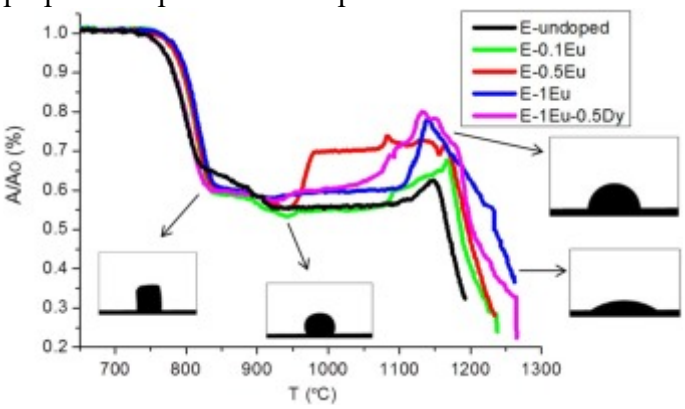

Fig. 4. HSM of the E glass powders. Heating rate:10 °C/min.

Table 4. Sintering and flow temperatures of the E glasses from HSM.

Samples	T_{FS}(°C) ± 10	T_{MS1}(°C) ± 10	T_{MS2}(°C) ± 10	T_S(°C) ± 10	Sphere(°C) ± 10	T_{HB}(°C) ± 3	T_F(°C) ± 3
E-undoped	761	814	923	860	910	1164	–
E-0.1 Eu	765	832	915	870	931	1210	1241
E-0.5 Eu	767	835	932	871	940	1210	–
E-1 Eu	765	840	904	880	1147	1210	–
E-1 Eu - 0.5Dy	752	835	918	871	940	1197	1260

3.2. X-ray diffraction

Fig. 5 shows the X-ray diffraction patterns of the doped glass-ceramics treated at 1100 °C for 1 h. The main crystalline peaks correspond to Sr-akermanite $Sr_2MgSi_2O_7$ (ICDD: 75–1736). Other very small peaks also appear in the E glass-ceramics whereas a cleaner diffractogram is obtained when melting in a gas furnace; the G-1 Eu-0.5Dy glass-ceramic diffractogram is shown as an example. Similar diffractograms were obtained after 1 h or 1 min of treatment at 1100 °C.

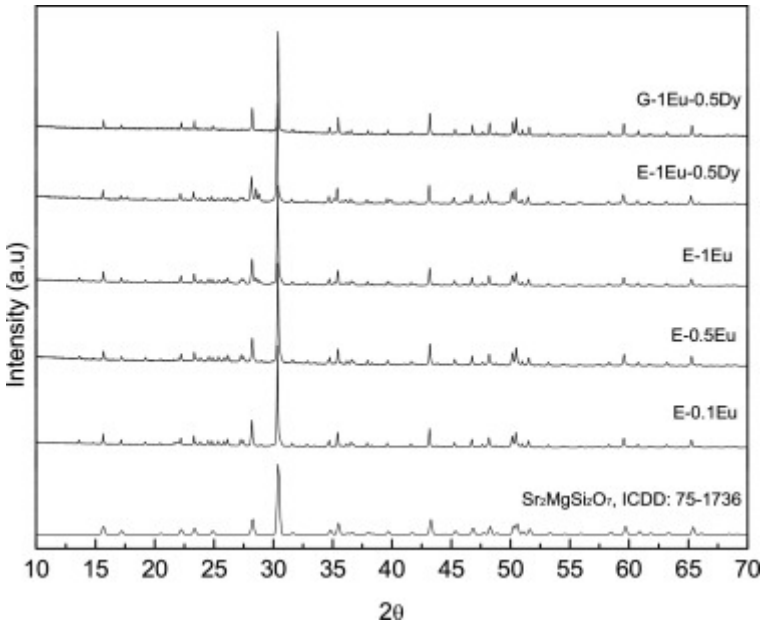

Fig. 5. XRD patterns of doped glass-ceramic samples treated at 1100 °C for 1 h.

Considering the initial theoretical glass composition (55SiO_2-27SrO-18MgO mol%.) and the main crystallized phase ($Sr_2MgSi_2O_7$), the maximum percentage of crystalline phase that may be obtained is 73 wt%. If the analysed compositions are taken into account (Table 3), maximum percentages of 80, 74 and 67 wt% for E-0.5 Eu, E-1 Eu-0.5Dy and G-1 Eu-0.5Dy, respectively, have been calculated.

To determine the crystallized fraction in these selected glass-ceramics, quantitative Rietveld refinement was performed with XRD data adding NaF as internal weight standard employing a methodology described previously [42].

Figs. 6 a, b and c show the Rietveld refinement diffraction profiles for the glass-ceramics E-0.5 Eu, E-1 Eu-0.5Dy and G-1 Eu-0.5Dy. The amount of crystalline fraction of $Sr_2MgSi_2O_7$ was determined to be 37, 30 and 22 wt% for these three samples, respectively (Table 5). The E glass-ceramics also contain a small amount of other crystalline phases. For the composition G-1 Eu-0.5Dy, $Sr_2MgSi_2O_7$ is the only crystalline phase and the composition of the rather large remaining glassy phase (78.5 wt%) can then be calculated giving 47.2SiO_2.14.5SrO.15.4MgO wt% (60.1SiO_2 10.7SrO 29.2MgO mol%). Selected structural information of the refined $Sr_2MgSi_2O_7$ phase is provided in Table 6.

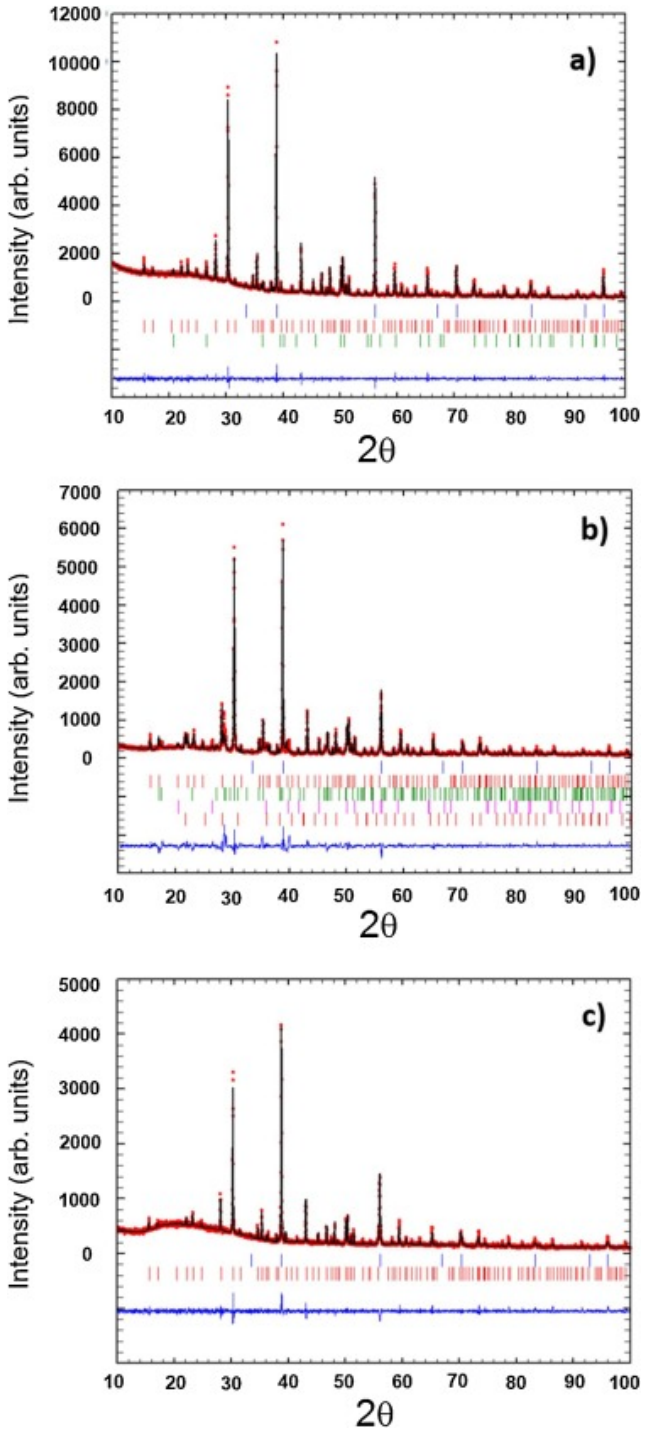

Fig. 6. Observed (red circles), calculated (black continuous line) and difference (continuous blue line at bottom) X-ray powder diffraction profiles of glass-ceramics with NaF as internal weight standard: a) E-0.5 Eu glass-ceramic with Bragg peaks of NaF, $Sr_2MgSi_2O_7$ and SiO_2 (quartz) indicated by top, middle and bottom vertical bars, respectively; b) E-1 Eu-0.5Dy glass-ceramic with the Bragg peaks of NaF, $Sr_2MgSi_2O_7$, $Sr(OH)_2$, quartz and cristobalite indicated from top to bottom vertical bars, respectively; c) G-1 Eu-0.5Dy glass-ceramic with the Bragg peaks of NaF and $Sr_2MgSi_2O_7$ indicated by top and bottom vertical bars, respectively. (For interpretation of the references to colour in this figure legend, the reader is referred to the web version of this article.)

Table 5. Weight percentages of crystallized phases obtained from Rietveld Refinement.

Sample	$Sr_2MgSi_2O_7$	$Sr(OH)_2$	SiO_2 quartz	SiO_2 cristobalite	Crystallised	Amorphous
E-0.5 Eu	36.6	–	1.45	–	38.1	61.9
E-1 Eu-0.5Dy	29.6	10.8	4.9	5.1	50.4	49.6
G-1 Eu-0.5Dy	21.5	–	–	–	21.5	78.5

Table 6. Cell parameters of the principal $Sr_2MgSi_2O_7$ phase (space group $P4^{-}21m$) obtained from Rietveld Refinement ($\alpha=\beta=\gamma=90°$).

Cell Parameters(Å)	E-0.5 Eu	E-1 Eu-0.5Dy	G-1 Eu-0.5Dy
a = b	7.9956 (2)	8.0039(6)	8.0062(5)
c	5.1593(2)	5.1606(4)	5.1687(4)

3.3. SEM-CL

On exposure to UV radiation ($\lambda = 365$ nm), the glasses show red luminescence and the corresponding glass-ceramics blue luminescence. Once the UV lamp is switched off, the blue emission does not persist in the glass-ceramic samples doped only with Eu. Only the composition G-1 Eu-0.5Dy shows persistence for a time of 2 min observed by the naked eye (Fig. 7). The time of persistence increases under cooling up to a time of 5 min at 0 °C. When heated at 130 °C the sample shows red emission (without persistence) under UV light (Fig. 7). This effect is reversible as the cooled glass-ceramic pellet re-emits in blue with the same persistence.

Fig. 7. G-1 Eu-0.5Dy glass-ceramic pellets under UV light (365 nm) a) lamp on b) lamp off c) the same glass-ceramic showing red emission under heating at 130 °C, lamp on. (For interpretation of the references to colour in this figure legend, the reader is referred to the web version of this article.)

The glass-ceramic microstructure and the crystals responsible for the emission can be observed using the panchromatic CL images. All the images correspond to the surface of a polished pellet with the microscope focused on the central part of the pellet. Figs. 8a, b and c show the E-0.5 Eu, E-1 Eu-0.5Dy and G-1 Eu-0.5Dy glass-ceramics, the same samples analysed by Rietveld refinement. In the images presented below, SEM

images (black and white) and panchromatic images (green) corresponding to the same area of the pellet are compared.

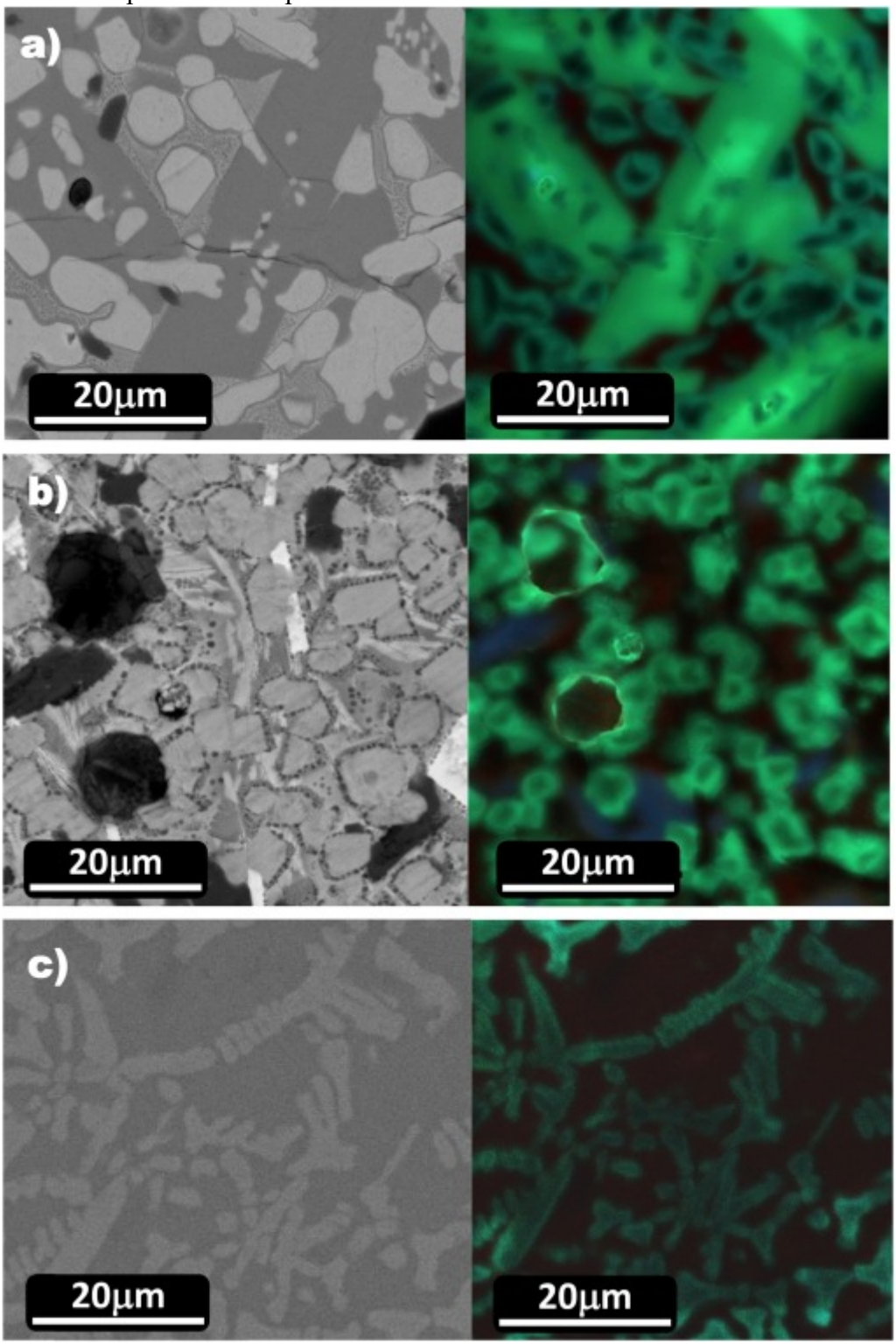

Fig. 8. SEM-CL images of a) E-0.5 Eu, b) E-1 Eu-0.5Dy and c) G-1 Eu-0.5Dy glass-ceramics.

Comparison of the samples melted in the electric furnace shows that the co-doped sample exhibits smaller crystals with lower fraction of vitreous phase. The crystals in

the co-doped sample melted in the gas furnace presents a more ordered dendritic structure with respect to the same material melted in the electric furnace. The glass composition obtained with the gas furnace had lower Sr content (20 %) than the theoretical composition, which, together with the different melting atmosphere and the incorporation of Al_2O_3 and ZrO_2 from the crucible, greatly affects the crystallization. It is evident how, in glass melted in an electric furnace, the green emission originates from the edge of the crystals, while in the gas furnace melted glass the emission comes from the interior of the crystals.

The SEM image of E-0.5 Eu, Fig. 9, shows different phases and a dark contrasted area of material in which Eu was not detected. Table 7 provides the analysis of the chemical composition of each zone measured by EDX. Point 2 corresponds to the main phase observed by XRD, $Sr_2MgSi_2O_7$, which contains a small amount of europium. Nevertheless, the green emission does not come from the interior of the crystals, but rather their surface. Point 3 is a phase around the crystals with a higher SiO_2/SrO ratio which contains most of the europium. Point 1 resembles the remaining glassy phase in which no Eu content could be detected. The secondary phase (SiO_2 quartz) in this glass-ceramic cannot be seen in this figure but does not contribute to the observed luminescence.

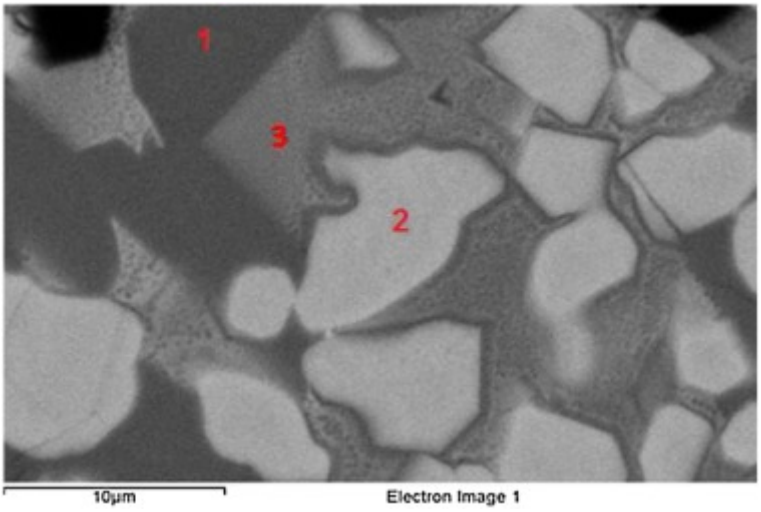

Fig. 9. SEM image of the E-0.5 Eu glass-ceramic.

Table 7. Compositional analysis (wt%) of E-0.5 Eu glass-ceramic as determined by EDX corresponding to Fig. 9.

	Theoretical glass composition	**1**	**2 $Sr_2MgSi_2O_7$**	**3**
MgO	8.92	9.78	9.02	5.29
SiO_2	39.81	59.18	36.33	62.68
SrO	49.25	31.04	54.23	20.19
Eu_2O_3	2.02	–	0.43	11.83

The SEM image of E-1 Eu-0.5Dy, Fig. 10, also shows different areas. Table 8 lists the analysed chemical composition of each zone determined by SEM-CL-EDX. Point 2 corresponds to the crystals of the main $Sr_2MgSi_2O_7$ phase (with diameter in the range 2−7 μm), containing a small amount of europium responsible for the emission coming from the borders of the crystals. Point 3 is again a phase with a higher SiO_2/SrO ratio containing both europium and dysprosium. Point 1 is a strontium-rich phase that likely corresponds to the $Sr(OH)_2$ quantified by Rietveld refinement in this sample. A higher concentration of europium and dysprosium is also detected in this phase. Finally, point 4 is a silica-rich phase that likely corresponds to the quartz and cristobalite determined by XRD and quantified by Rietveld refinement. $Sr(OH)_2$ and silica phases do not contribute to the observed luminescence.

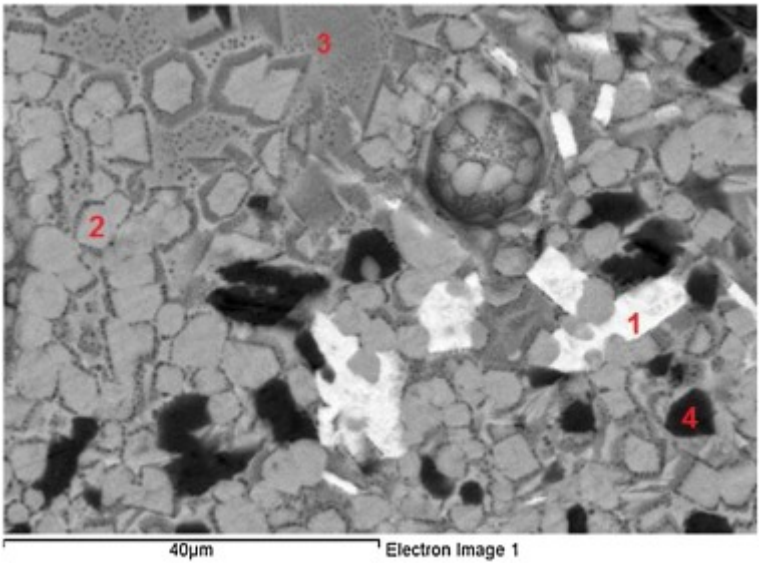

Fig. 10. SEM image of the E-1 Eu-0.5Dy glass-ceramic.

Table 8. Compositional analysis (wt%) of E-1 Eu-0.5Dy glass-ceramic as determined by EDX corresponding to Fig. 10.

	Theoretical glass composition	**1**	**2 $Sr_2MgSi_2O_7$**	**3**	**4**
MgO	8.55	–	9.94	8.84	35.34
SiO_2	38.18	37.88	36.41	58.63	61.49
SrO	47.23	30.90	52.74	23.32	3.17
Eu_2O_3	3.88	22.57	0.92	6.38	–
Dy_2O_3	2.15	8.65	–	2.83	–

The SEM image of G-1 Eu-0.5 Dy, Fig. 11, shows only two phases. Table 9 provides analysis of the chemical composition of each zone measured by EDX. Point 2 corresponds to crystalline $Sr_2MgSi_2O_7$ responsible for the green emission, although most of the rare earth is concentrated in the residual glassy phase (point 1).

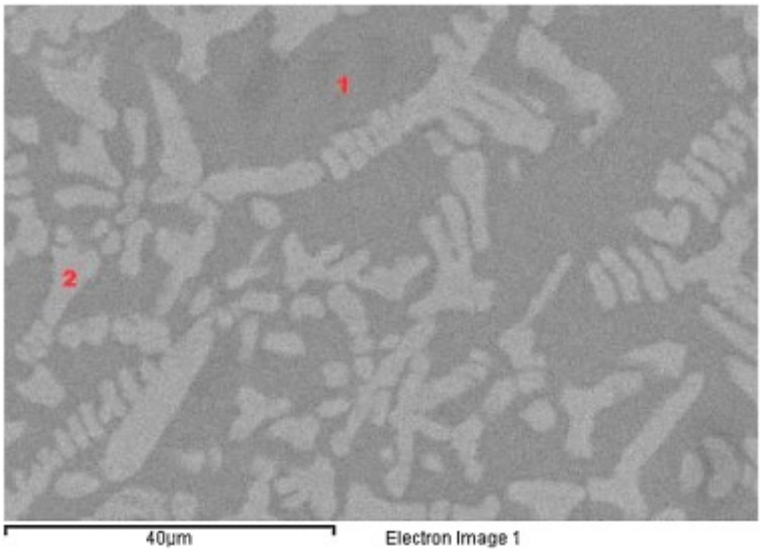

Fig. 11. SEM image of the G-1 Eu-0.5Dy glass-ceramic.

Table 9. Compositional analysis (wt%) of G-1 Eu-0.5Dy glass-ceramics as determined by EDX corresponding to Fig. 11.

	Theoretical glass composition	**1**	**2 $Sr_2MgSi_2O_7$**
MgO	8.55	8.35	9.01
SiO2	38.18	51.42	36.70
SrO	47.23	26.87	53.08
Al_2O_3	–	3.72	1.21
Eu_2O_3	3.88	6.99	–
Dy_2O_3	2.15	2.64	–

The spectrally resolved CL images of the G-1 Eu-0.5Dy glass-ceramic are shown in Fig. 12; the monochromatic images reveal the emission of the different phases. Three main areas of the sample have been analysed and their corresponding emission spectra are shown in Fig. 13. Spectra 1 and 3 are associated with the area of the sample where there are no crystals (remaining glassy phase) and exhibit a maximum peak at 615 nm corresponding to the typical red emission of Eu^{3+}. Zone 2 (spectrum 2) corresponds to the light-grey crystals responsible for the green-blue emission where the akermanite phase $Sr_2MgSi_2O_7$ appears; spectrum 2 exhibits a maximum peak at 484 nm corresponding to the typical blue emission of Eu^{2+}.

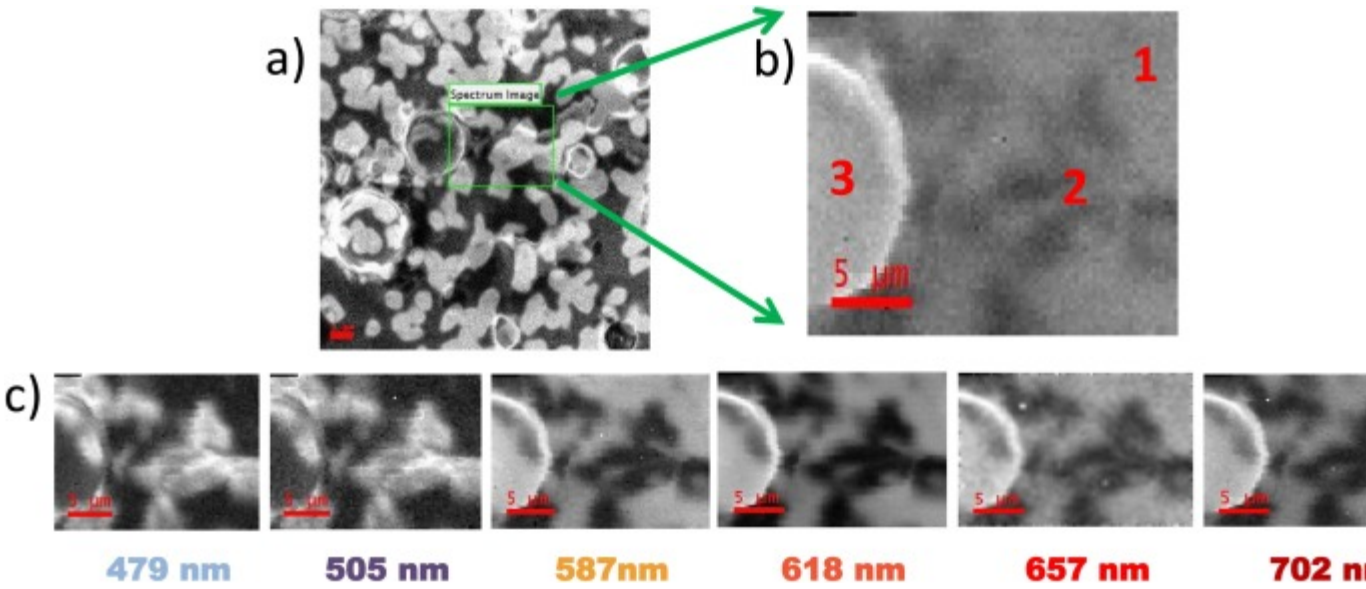

Fig. 12. SEM of a) hyperspectral-CL image, b) monochromatic image and c) emission at different wavelengths under electron beam for G-1 Eu-0.5Dy glass-ceramic.

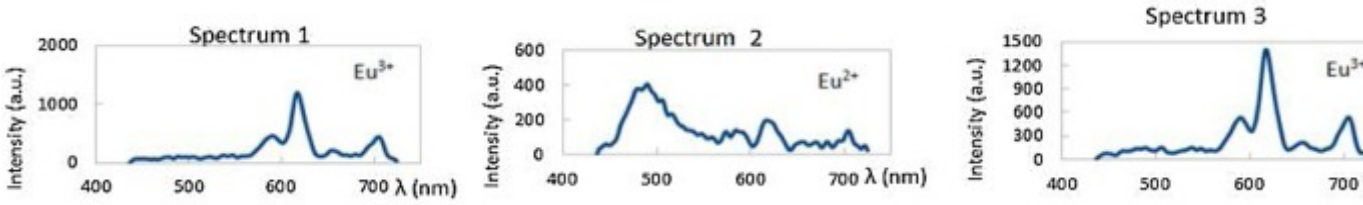

Fig. 13. SEM-CL spectra of the points 1, 2 and 3 marked in Fig.12, corresponding to different regions of the G-1 Eu-0.5Dy glass-ceramics.

3.4. Optical properties

Fig. 14a shows the excitation spectra monitored at 476 nm and 613 nm for E-0.5 Eu glass-ceramics. For the spectra collected at 476 nm, one Eu^{2+} excitation broad band is observed at 341 nm, whereas, for the spectra collected at 613 nm, two Eu^{3+} excitation bands occur at 394 nm and 465 nm. Both Eu^{3+} and Eu^{2+} emissions contribute to the luminescence of the E-0.5 Eu glass-ceramic. Fig. 14b displays the emission spectra for the E-0.5 Eu glass-ceramic at an excitation wavelength of 394 nm with two fluorescence emissions at 465 nm and 613 nm. Under excitation at 341 nm, only one fluorescence band is observed at 484 nm, ascribed to an Eu^{2+} emission.

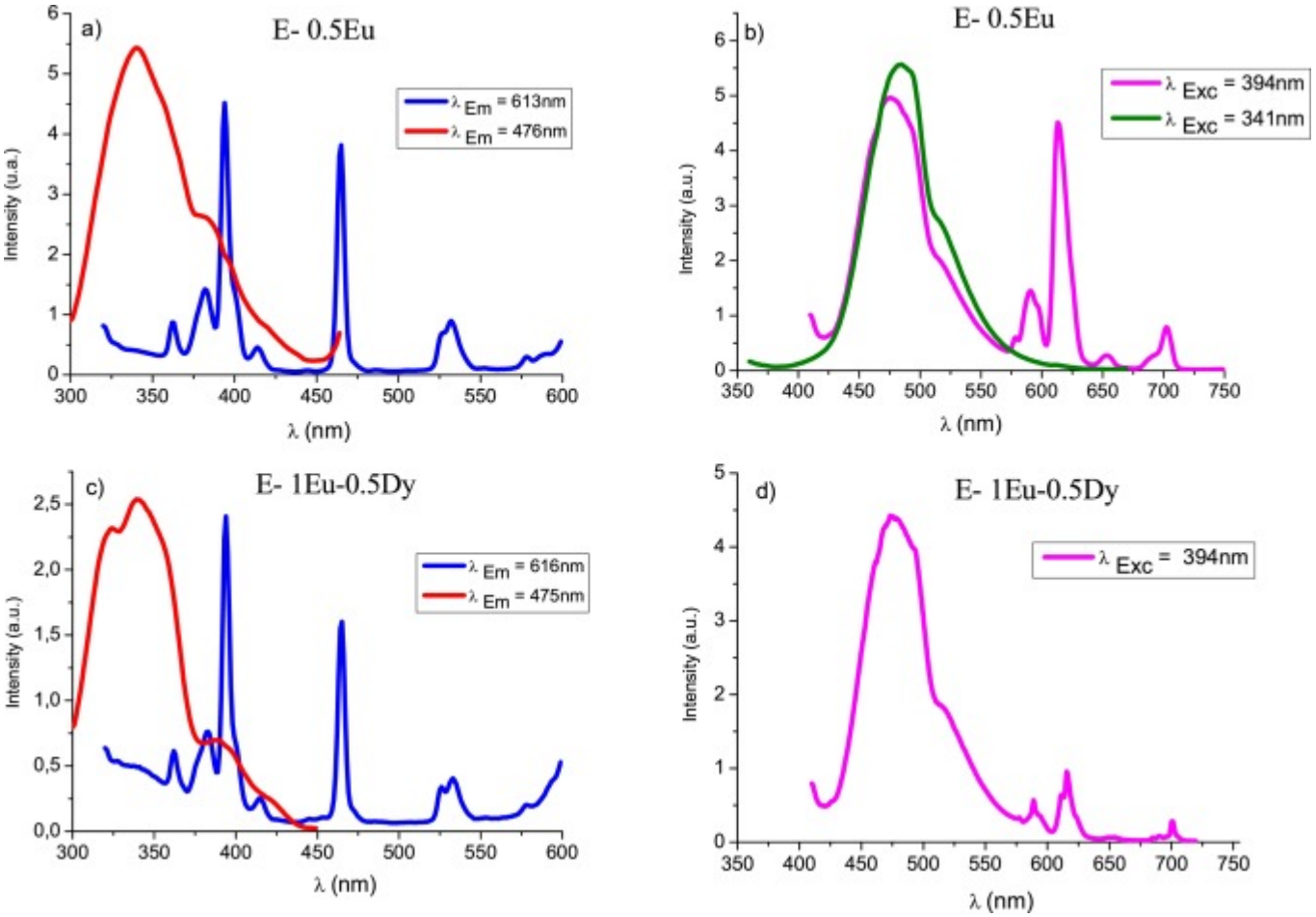

Fig. 14. Excitation and emission spectra of a), b) E-0.5 Eu and c), d) E-1 Eu-0.5Dy glass-ceramics.

Fig. 14c presents the excitation spectra monitored at 475 nm and 616 nm for E-1 Eu-0.5Dy glass-ceramics. For the spectra collected at 475 nm, one excitation broad band is observed at 341 nm from Eu^{2+}, while for the spectra collected at 616 nm two excitation bands of cations Eu^{3+} were observed at 394 nm and 465 nm. Fig. 14d shows the emission spectra of the glass-ceramic with excitation wavelength at 394 nm and one fluorescence emission band at 465 nm.

Comparison of the spectra in Fig. 14b and 14d indicates that the 613/616 nm fluorescence emissions from the Eu^{3+} ions considerably decrease when dysprosium is used as a codopant.

Fig. 15 shows the emission spectra of the glass-ceramics G-0.5Dy, G-0.5 Eu and G-1 Eu-0.5Dy. G-0.5Dy, as expected, does not emit in afterglow because Dy^{3+} does not act as a luminescence centre as reported earlier [27,17]. The G-0.5 Eu glass-ceramic has an excitation wavelength of 372 nm, which shifts to 390 nm for the co-doped glass. The main peak at 484 nm is assigned to the Eu^{2+} transitions, and the other peaks are associated with transitions of the Eu^{3+} ion. These are assigned to the $T_{2g} \rightarrow {}^8S_{7/2}$ transition of Eu^{2+} ions in the crystals and to the ${}^5D_0 \rightarrow {}^7F_2$ transition in

Eu^{3+} from the glassy phase, respectively [34]. The signal intensity ratio between the emissions of Eu^{2+} and Eu^{3+} is smaller in the co-doped sample.

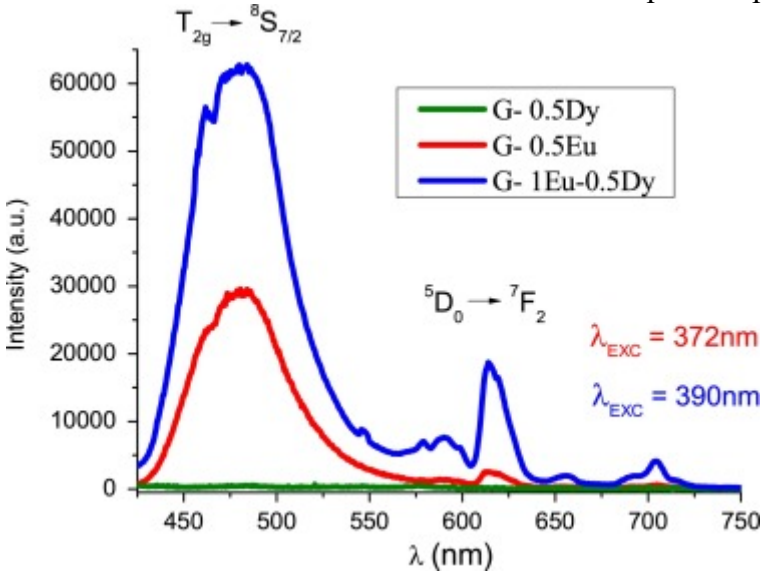

Fig. 15. Photoluminescence emission spectra of the G-0.5Dy, G-0.5 Eu and G-1 Eu-0.5Dy glass-ceramics.

Fig. 16a shows the life time registered at 4.5 °C from the G-1 Eu-0.5D glass-ceramic. The initial line indicates that the excitation source is on; on turning it off, the luminescence intensity begins to fall until it reaches zero. This experiment has been carried out at different temperatures, and a curve measured for each temperature. From these data, mathematical calculations have been made assuming that 100 % of the emission appears with the lamp on and subtracting different percentages of emission until reaching zero emission. Fig. 16b shows the lifetime decay at different temperatures, until the sample stops emitting; the times are shown in Table 10.

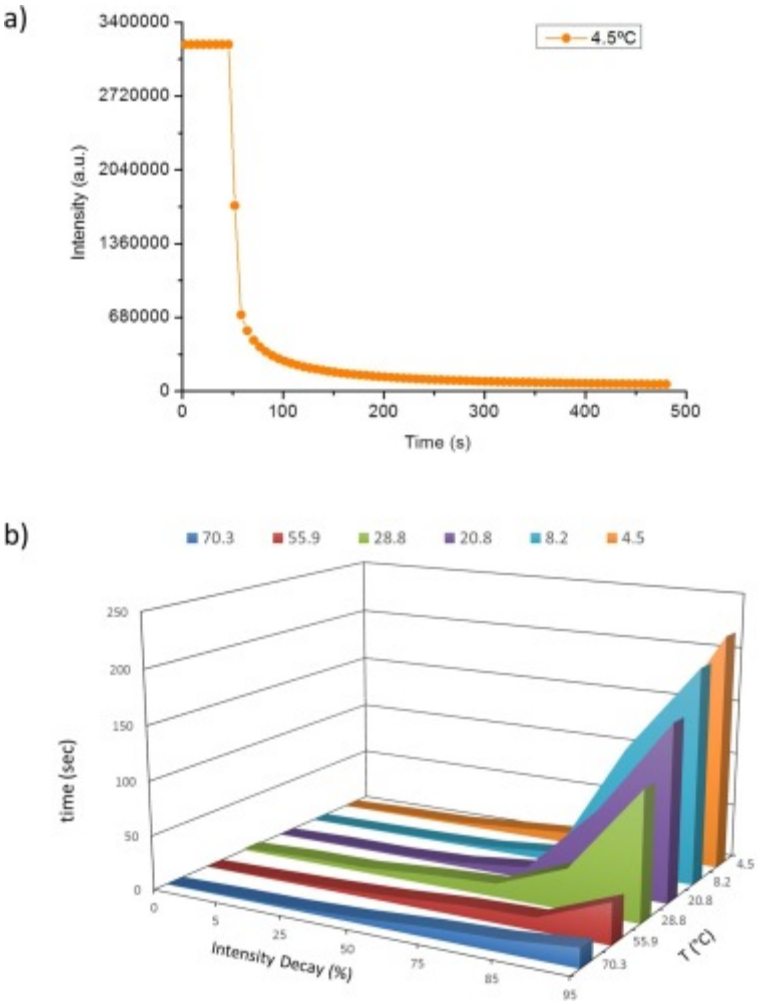

Fig. 16. a) Life time of the blue emission collected for the G-1 Eu-0.5D glass-ceramic and b) average lifetimes at different temperatures. (For interpretation of the references to colour in this figure legend, the reader is referred to the web version of this article.)

Table 10. Lifetimes of the G-1 Eu-0.5D glass-ceramic blue emission at different temperatures.

T (ºC)	**time (s)**
4.5	248.5
8.2	219.5
20.8	161.7
28.8	117.7
55.9	37.2
70.3	17.6

Several thermoluminescence studies of the $Sr_2MgSi_2O_7$ phase are reported in the literature [43]. Initially, the intensity increases with temperature until a maximum value is reached for a given temperature, and then decreases with a further increase in temperature. Rare-earth-ion doping is known to increase lattice defects that are already

present in the crystal. Thermoluminescence curves [44] indicate that, around 100 °C, post-luminescence properties increase due to deeper traps. Other studies [45] show that, at 80 °C, the curves show a strong thermoluminescence peak with much wider bands. Both studies indicated that Eu/Dy co-doping improves afterglow properties.

Fig. 17 shows the afterglow spectra of the G-1 Eu-0.5D glass-ceramics. In this figure, the samples show broad emission bands reaching a peak of about 470 nm associated with the Eu^{2+} from the crystalline phase. In addition, another emission at 750 nm is associated with the Eu^{3+} in the remaining glassy phase. It is important to mention that the surface of the samples after the crystallization thermal treatment is glassy. It is observed that, as the temperature of the sample increases, the intensity of the band at 470 nm gradually decreases while the intensity of the band at 750 nm remains constant. This result explains the increase in persistence as the temperature decreases and also the change in colour observed in the blue-red emission as the sample temperature increases. The Eu^{3+} in the remaining glassy phase causes the predominance of the red emission when heating the sample. This red-blue emission change is reversible with heating and cooling and is, therefore, an interesting property for temperature sensors. Nevertheless, at the same time, the significant contribution of the red emission coming from the glassy phase hinders the persistence of the blue emission of the glass-ceramics.

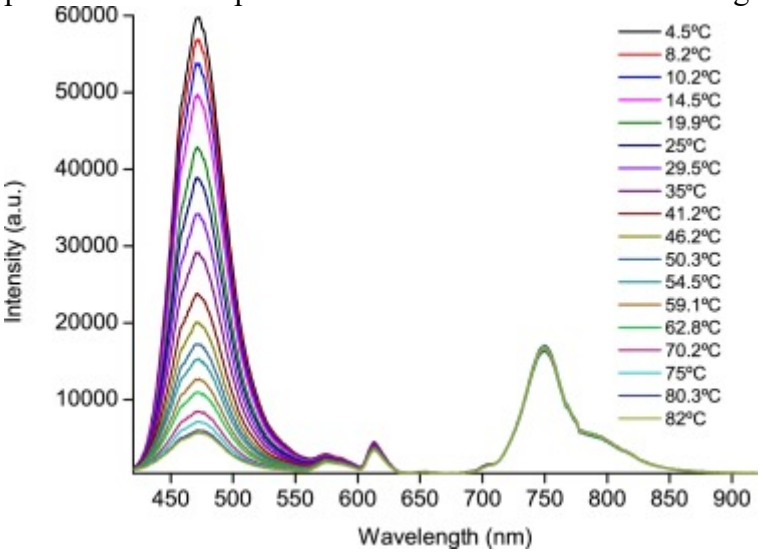

Fig. 17. Afterglow spectra of G-1 Eu-0.5Dy glass-ceramic at different temperatures.

In this work, CL and PL measurements have confirmed that Eu^{2+} is obtained in a non-reducing atmosphere through the presence of tetrahedral anionic groups such as those present in the crystalline phase $Sr_2MgSi_2O_7$ of the studied glass-ceramics after the crystallization process of the glass [26,28]. Both Eu^{3+} and Eu^{2+} emissions are observed in these materials with the former arising from the crystalline phase. The persistence of

the luminescence of the co-doped glass-ceramics with Dy is remarkably dependent on the glass-ceramic final microstructure. The green emission in the glass-ceramic obtained from melting in an electric furnace emanates from the edge of the circular $Sr_2MgSi_2O_7$ crystals; other minor and non-desirable crystalline phases are also present. In the glass-ceramic obtained from melting in a gas furnace, only the relevant phase is present and the green emission comes from the interior of the dendritic crystals. In this last case, the amount of remaining glassy phase is higher and the persistence is the highest observed.

In future work, the concentration of Eu and Dy will be optimized together with a deeper study of the influence of the composition on the crystallization mechanism, size, shape and amount of the crystals, and the partitioning of the rare-earth ions between glass-matrix and crystalline phase. These parameters control the relative intensities of both blue and red emissions and highly influence the persistence of the blue emission. Moreover, $Sr_2MgSi_2O_7$ crystals have the capacity to generate oxygen and strontium vacancies. The intensity of the post-luminescence of persistent phosphors depends on the electron densities of the traps, while the duration of the post-luminescence depends on the depth of the trapped electrons [43]. It is believed that these vacancies are major contributors to the phosphorescence behaviour of many oxide-based phosphors and relevant research is underway using neutron diffraction and XAS.

4. Conclusions

Glass-ceramics based on the Eu/Dy-doped $Sr_2MgSi_2O_7$ phosphor have been obtained from sintering and crystallization of glass powders. The increase in dopant content resulted in increased stability of the glass versus crystallization. Electric and gas furnaces were employed for glass melting without use of reducing agents. The as-prepared glasses doped with Eu and co-doped with Eu/Dy exhibit red emissions; moreover, after thermal treatment the corresponding glass-ceramics emit in blue under excitation by UV light. The composition G-1 Eu-0.5Dy shows the greatest persistence results for the blue emission.

The different conditions of electric and gas furnaces influence the final chemical composition which considerably affects the crystallization process giving rise to $Sr_2MgSi_2O_7$ glass-ceramics with very different microstructure which, in turn, has a significant influence on the luminescence and persistence properties. The glasses melted in an electric furnace led to the crystallization of other phases, including quartz.

The emission spectra of the glass-ceramics exhibit features attributable to both Eu^{2+} and Eu^{3+} cations. The glass-ceramic co-doped with Eu_2O_3/Dy_2O_3 provided a signal associated with Eu^{3+} smaller than that of the glass-ceramic doped only with Eu^{2+}. CL measurements indicate that Eu^{2+} emission originates from the $Sr_2MgSi_2O_7$ crystals and the Eu^{3+} emission from the remaining glassy phase, suggesting that the reduction of europium occurs in the crystalline phase.
It was demonstrated that the use of Dy as a co-dopant increases the persistence of luminescence. The final material is sensitive to temperature, modifying the persistence time and red-blue luminescence, rendering these materials suitable for thermal sensors.

Summary of novel conclusions

- Glass-ceramics based on the Eu/Dy-doped $Sr_2MgSi_2O_7$ phosphor have been obtained from sintering and crystallization of glass powders. Electric and gas furnaces were employed for glass melting without use of reducing agents. The doped parent glasses show red emission under excitation of UV light whereas the corresponding glass-ceramics show blue emission.
-The different conditions of the electric and gas furnaces influence the final chemical composition which considerably affects the crystallization process giving rise to $Sr_2MgSi_2O_7$ glass-ceramics with very different microstructures which, in turn, has a significant influence on the luminescence and persistence properties.
-Co-doped glass-ceramics melted in a gas furnace show the highest persistence for blue emission. The material is sensitive to temperature, which modifies the persistence time and red-blue luminescence, rendering these materials suitable for thermal sensors.

Declaration of Competing Interest

The authors declare that they have no known competing financial interests or personal relationships that could have appeared to influence the work reported in this paper.

Acknowledgements

Funding from MINECO under project MAT2017-87035-C2-1-P/2-P (AEI/FEDER, UE) and from PID2019-107439GB-I00 project is acknowledged.

References

1. M.T. Fernández-Argüelles, J.R. Encinar, A. Sanz-Medel, J.M. Costa-Fernández

Phosphorescence. Principles and Instrumentation; Encyclopedia Analytic. Sci. (Second Edition), 8 (2005), pp. 149-157
2. J. Xu, S. Tanabe; Persistent luminescence instead of phosphorescence: history, mechanism, and perspective; J. Lumin., 205 (2018), pp. 581-620, 10.1016/j.jlumin.2018.09.047
3. K. Van Den Eeckhout, D. Poelman, P.F. Smet; Persistent Luminescence in Non-Eu^{2+}-Doped Compounds: A Review (2013), pp. 2789-2818, 10.3390/ma6072789
4. K.B. Lin, Y.H. Su; Photoluminescence of Cu:ZnS, Ag:ZnS, and Au:ZnS nanoparticles applied in Bio-LED; Appl. Phys. B Lasers Opt., 113 (2013), pp. 351-359, 10.1007/s00340-013-5497-z
5. R.E. Rojas-Hernández, F. Rubio-Marcos, M.Á. Rodriguez, F. Fernández Long lasting phosphors: $SrAl_2O_4$: Eu, Dy as the most studied material Renew. Sustain. Energy Rev. (2017), pp. 1-12, 10.1016/j.rser.2017.06.081
6. Y. Lin, Z. Tang, Z. Zhang, C.W. Nan; Luminescence of Eu^{2+} and Dy^{3+} activated $R_3MgSi_2O_8$-based (R=Ca, Sr, Ba) phosphors; J. Alloys. Compd., 348 (2003), pp. 76-79, 10.1016/S0925-8388(02)00796-X
7. Y. Lin, C.W. Nan, X. Zhou, J. Wu, H. Wang, D. Chen, S. Xu; Preparation and characterization of long afterglow $M_2MgSi_2O_7$-based (M: Ca, Sr, Ba) photoluminescent phosphors; Mater. Chem. Phys., 82 (2003), pp. 860-863, 10.1016/j.matchemphys.2003.07.015
8. J. Qiu, K. Hirao; Long lasting phosphorescence in Eu^{2+}-doped calcium aluminoborate glasses; Solid State Commun., 106 (1998), pp. 795-798, 10.1016/S0038-1098(98)00134-3
9. T. Matsuzawa; A new long phosphorescent phosphor with high brightness, $SrAl_2O_4$:Eu^{2+},Dy^{3+}; J. Electrochem. Soc., 143 (1996), p. 2670, 10.1149/1.1837067
10. R. Sakai, T. Katsumata, S. Komuro, T. Morikawa; Effect of composition on the phosphorescence from $BaAl_2O_4$: Eu^{2+}, Dy^{3+} crystals; J. Lumin., 85 (1999), pp. 149-154, 10.1016/S0022-2313(99)00061-7
11. K. Van Den Eeckhout, P.F. Smet, D. Poelman; Persistent Luminescence in Eu^{2+}-Doped Compounds: A Review (2010), pp. 2536-2566, 10.3390/ma3042536
12. V. Abbruscato; Optical and electrical properties of $SrAl_2O_4$:Eu^{2+}; J. Electrochem. Soc., 118 (1971), p. 930, 10.1149/1.2408226
13. T. Aitasalo, J. Hassinen, J. Hölsä, T. Laamanen, M. Lastusaari, M. Malkamäki, J Niittykoski, P. Novák; Synchrotron radiation investigations of the $Sr_2MgSi_2O_7$:Eu^{2+},R^{3+} persistent luminescence materials; J. Rare Earths., 27 (2009) pp. 529-538, 10.1016/S1002-0721(08)60283-5
14. T. Aitasalo, P. Dereń, J. Hölsä, H. Jungner, J.C. Krupa, M. Lastusaari, J. Legend ziewicz, J. Niittykoski, W. Stręk; Persistent luminescence phenomena in materials doped with rare earth ions; J. Solid State Chem., 171 (2003), pp. 114-122, 10.1016/S0022-4596(02)00194-9
15. P. Dorenbos; Locating lanthanide impurity levels in the forbidden band of host crystals; J. Lumin., 108 (2004), pp. 301-305, 10.1016/j.jlumin.2004.01.064
16. F. Clabau, X. Rocquefelte, S. Jobic, P. Deniard, M. Whangbo, A. Garcia, J. Rou xel; Mechanism of phosphorescence appropriate for the long-lasting phosphors Eu^{2+d}oped SrAl2O_4 with codopants Dy^{3+} and B^{3+}; Chem. Mater., 2 (2005), pp. 3904-3912

17. O. Hai, H. Jiang, Q. Zhang, Q. Ren, X. Wu, J. Hu; Effect of cooling rate on the microstructure and luminescence properties of $Sr_2MgSi_2O_7:Eu^{2+},Dy^{3+}$ materials Luminescence (2017), pp. 1-6, 10.1002/bio.3343
18. Y. Gong, Y. Wang, Y. Li, X. Xu, W. Zeng; Fluorescence and phosphorescence properties of new long-lasting phosphor $Ba_4(Si_3O_8)_2$ Eu^{2+}, Dy^{3+}; Opt. Express, 19 (2011), pp. 4310-4315
19. T. Aitasalo, A. Hietikko, J. Hölsä, M. Lastusaari, J. Niittykoski, T. Piispanen Crystal structure of the $Ba_3MgSi_2O_8:Mn^{2+},Eu^{2+}$ phosphor for white light emitting diodes; European Powder Diffraction Conference, EPDIC 10. doi: https://doi.org/10.1524/9783486992540-072 (2007), pp. 461-466
20. H.K. Jung, K.S. Seo; Luminescent properties of Eu^{2+}-activated (Ba, $Sr)_3MgSi_2O_8$ phosphor under VUV irradiation; Opt. Mater. (Amst)., 28 (2006), pp. 602-605, 10.1016/j.optmat.2005.09.027
21. T. Nakanishi, S. Tanabe; Preparation of $BaSi_2O_5:Eu^{2+}$ glass ceramic phosphors and luminescent properties; Journal of Light & Visual Environment, (2) (2008), pp. 93-96, 10.2150/jlve.32.93
22. K. Asami, J. Ueda, S. Tanabe; Long persistent luminescence and blue photochromism in Eu^{2+}-Dy^{3+} co-doped barium silicate glass ceramic phosphor; J. Lumin., 207 (2019), pp. 246-250, 10.1016/j.jlumin.2018.11.006
23. X. Wei, Y. Shen, G. Zuo, L. Hou, Y.Z. Meng, F. Li; Preparation of porous $Sr_2MgSi_2O_7:Eu^{2+},Dy^{3+}$ energy storage carriers via sol-hydrothermal synthesis Ceram. Int., 41 (2015), pp. 13872-13877, 10.1016/j.ceramint.2015.06.144
24. W. Pan, G. Ning, X. Zhang, J. Wang, Y. Lin, J. Ye; Enhanced luminescent properties of long-persistent $Sr_2MgSi_2O_7:Eu^{2+}$, Dy^{3+} phosphor prepared by the co-precipitation method; J. Lumin., 128 (2008), pp. 1975 -1979 10.1016/j.jlumin.2008.06.009
25. H. Duan, Y.Z. Dong, Y. Huang, Y.H. Hu, X.S. Chen; The important role of oxygen vacancies in $Sr_2MgSi_2O_7$ phosphor; Phys. Lett. A, 380 (2016), pp. 1056-1062, 10.1016/j.physleta.2016.01.001
26. B. Yuan, Y. Song, L. Kong, C. Dai, H. Zou; The sensitized luminescence and tunable color of single-component $Sr_2MgSi_2O_7:Bi^{3+}/Sm^{3+}/Tb^{3+}$ phosphor via energy transfer for white-light emitting diodes; Phys. B Condens. Matter. 550 (2018), pp. 75-89, 10.1016/j.physb.2018.09.001
27. Z. Pei, Q. Zeng, Q. Su; The application and a substitution defect model for Eu^{3+} Eu^{2+} reduction in non-reducing atmospheres in borates containing BO_4 anion groups; J. Phys. Chem. Solids, 61 (2000), pp. 9-12
28. A.J. Fernández-Carrión, K. Al Saghir, E.Veron, A. Becerro, F. Porcher, W. Wisniewski, G. Matzen, F. Fayon, M. Allix; Local disorder and tunable luminescence in $Sr_{1-x/2}Al_{2-x}Si_xO_4$ ($0.2 \leq x \leq 0.5$) transparent ceramics Inorg. Chem., 56 (2017), pp. 14446-14458, 10.1021/acs.inorgchem.7b01881
29. L. He, B. Jia, L. Che, W. Li, W. Sun; Preparation and optical properties of afterglow $Sr_2MgSi_2O_7$: Eu^{2+}, Dy^{3+} electrospun nano fibers; J. Lumin., 172 (2016), pp. 317-322, 10.1016/j.jlumin.2015.12.012
30. Chen, T. Chen; Sol-gel synthesis and the effect of boron addition on the phosphorescent properties of $SrAl_2O_4:Eu^{2+},Dy^{3+}$ phosphors; Mater. Res., 16 (3) (2001), pp. 644-651
31. C. Zhao, D. Chen, Y. Yuan, M. Wu; Synthesis of $Sr_4Al_{14}O_{25}$: Eu^{2+}, Dy^{3+} phosphor nanometer powders by combustion processes and its optical properties
Mater. Sci. Eng., 133 (2006), pp. 200-204, 10.1016/j.mseb.2006.06.042

32. J.P. Yong, J.K. Tack, H.C. Young, Y. Jung, H.J. Im, K. Song, Y.J. Kwang EPR investigation on a quantitative analysis of Eu(II) and Eu(III) in LiCl/KCl eutectic molten salt; Bull. Korean Chem. Soc., 29 (2008), pp. 127-129, 10.5012/bkcs.2008.29.1.127
33. S. Nishiura, S. Tanabe; Preparation and luminescence properties of glass ceramics precipitated with $M_2MgSi_2O_7:Eu^{2+}$ (M = Sr, Ca) phosphor for white light source; IEEE J. Sel. Top. Quantum Electron., 15 (2009), pp. 1177-1180, 10.1109/JSTQE.2009.2014175
34. V.A. Online, L. Wondraczek, S. Krolikowski, P. Nass; Europium partitioning, luminescence re-absorption and quantum efficiency in (Sr,Ca) ˚ akermanite–feldspar bi-phasic glass ceramics; J. Mater. Chem. C. (2013), pp. 4078-4086, 10.1039/c3tc30609g
35. M.J. Pascual, L. Pascual, A. Durán; Determination of the viscosity-temperature curve for glasses on the basis of fixed viscosity points determined by hot stage microscopy; Phys. Chem. Glas., 42 (2001), pp. 61-66
36. M.J. Pascual, M. Prado, A. Durán; A new method for determining fixed viscosity points of glasses; Phys. Chem. Glasses, 46 (5) (2005), pp. 512-520
37. W.L. Bragg; Crystal structure; Nature (1920)
38. Zalkin, D.H. Templeton; Refinement of the trigonal crystal structure of lanthanum trifluoride with neutron diffraction data, Acta Crystallogr Sect. B., 41 (1985), pp. 91-93, 10.1107/S0108768185001689
39. J. Rodríguez-Carvajal; Recent advances in magnetic structure determination by neutron powder diffraction; Phys. B Phys. Condens. Matter., 192 (1993), pp. 55-69, 10.1016/0921-4526(93)90108-I
40. S. Rodríguez López; Propiedades termomecánicas de sellos vitrocerámicos del sistema $RO-MgO-B_2O_3-SiO_2$ (R=Ba, Sr) para SOFC. PhD thesis; UAM (2016)
41. K. Matusita, S. Sakka; Kinetic study of crystallization of glass by differential thermal analysi-criterion on application of Kissinger plot; J. Non. Solids, 39 (1980), pp. 741-746
42. A De Pablos-Martín, N Hémono, G C Mather, S Bhattacharyya, T Höche, H Bornhöft, J Deubener, F Muñoz, A Durán, M J Pascual, Crystallization kinetics of LaF3 nanocrystals in an oxyfluoride glass, J. Am. Ceram. Soc. 94 (2011) 2420–2428, doi:10.1111/j.1551-2916.2011.04547.x
43. I.P. Sahu, D.P. Bisen, N. Brahme, R.K. Tamrakar; Enhanced luminescence performance of $Sr_2MgSi_2O_7:Eu^{2+}$ blue long persistence phosphor by co-doping with Ce^{3+} ions; J. Mater. Sci. Mater. Electron., 27 (2016), pp. 554-569, 10.1007/s10854-015-3789-2
44. X. Wang, F. Li, G. Zuo, Y. Shen, F. Li; Enhanced afterglow properties of Nd^{3+} co-doped $Sr_2MgSi_2O_7$: Eu^{2+}, Dy^{3+} synthesized by sol – gel method Ceram. Int., 42 (2016), pp. 19441-19444, 10.1016/j.ceramint.2016.09.051
45. H.A.I. Ou, J. Hongyi, X.U. Dong, W. Yahui, Z. Wei, L.U.O. Ting; Interaction of rare earth ions in $Sr_2MgSi_2O_7:Eu^{2+}$, Dy^{3+} material; J. Wuhan Univ. Technol. Sci. Ed. (2016), pp. 269-273, 10.1007/s11595-016-1363-2